2019 International Conference on Robotics and Automation (ICRA)
Palais des congres de Montreal, Montreal, Canada, May 20-24, 2019

Miniature Robotic Tubes with Rotational Tip-Joints as a Medical Delivery Platform

Rohith Karthikeyan, Shivanand Pattanshetti and Seok Chang Ryu

***Abstract*— We present a medical-needle-sized robotic tube with multi-degrees of freedom (M-DOF) rotational hinge joints at the instrument tip, fabricated by two-axis laser micro-machining. Due to the presence of an ample working channel and direct tip controllability, this tube is a potential candidate for the precise delivery of radioactive seeds, probes and micro-forceps to regions of interest within the human body. In this paper, the advantages of the proposed hinged instrument are studied in contrast with that of flexure joints, which include – fine angle control (posability), and a shorter joint length that enables compact articulation. In addition, the joint strength both in the axial and lateral directions was experimentally investigated to demonstrate its feasibility as a robust delivery platform. Further, the intuitive nature of hinge rotation permits the use of a simple kinematic model for accurate tip motion control, under fewer simplifying assumptions than flexure joints which are impeded by material non-linearity and geometric discontinuities. An instrumented prototype was used to test this model by delivering a laser beam along a prescribed path (synonymous to simple ablation tasks). The observed *RMS* position error for the projected beam was $\sim 0.364\ mm$.**

I. INTRODUCTION

Robot-assisted surgery has revolutionized how specific medical procedures are carried out since it was first introduced in the 1980s. Such robotic systems can filter hand tremors [1] and enable telesurgery, allowing surgeons to operate on a patient remotely. The commercially successful da Vinci (Intuitive Surgical, Sunnyvale, CA) is at the forefront of this market. As of 2018, the tools for the system are available in two sizes – 8 mm and 5 mm shaft diameters. However, with the evolving demands of surgical intervention, there is a need for smaller and functionally augmented instruments to improve task outcomes and safe operation [2].

Several small-scale continuum devices have been proposed, particularly for NOTES (Natural Orifice Transluminal Endoscopic Surgery), instruments including the HARP (Highly Articulated Robotic Probe) [3], tele-robotic systems [4], and the Flex Robotic System [5] have received considerable research attention from the medical robotics society. However, these instruments are limited by tool-size, the absence of a working channel for material and (or) device delivery, in particular, those necessary for some emerging medical techniques, among other constraints.

Concentric tube robots such as the ones proposed by Dupont et al. [6] remain among the more promising platforms and meet some of the functional requirements for tools within this scope. However, these designs are inherently unstable due to an actuation scheme that relies on physical interaction between sliding and rotating tubes. Small tip angle changes sometimes require complicated manipulations of the whole device. An asymmetrically patterned, robotic wrist presented in [7] offsets some of these limitations since it enables direct tip orientation control and a higher swept angle while retaining a central working channel. However, such goose-neck-type joints are unintuitive to control and lead to the loss of valuable workspace in spatially limited environments such as those encountered during pediatric surgery [8]. Further, the flexure joints are hampered by machining technique which may contribute to some mechanically and thermally induced residual stresses.

To address the above issues of size, function, and articulation, we propose a small instrument with rotational hinge joints that allow a greater angle between the tip and distal links, within a smaller workspace unlike flexures. Previously, we introduced a hinge joint fabricated on a small-sized tube (18 Ga BWG) by laser machining and studied the effect of design parameters on its range of motion [9]. In this paper, we verify the perceived merits of rotational hinge joints, and extend the investigation toward medically relevant utilities through kinematic analysis, tool strength characterization (for safe operation), and the demonstration of a functional working channel (targeted drug/ laser delivery). Towards

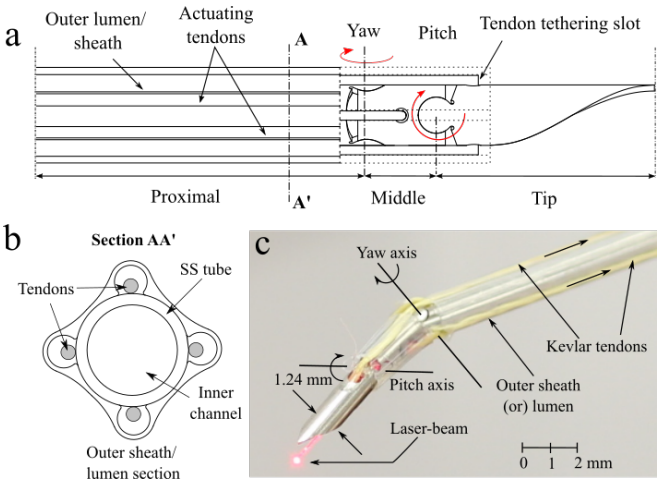

Fig. 1. Schematic and image of the proposed 2-DOF hinge-jointed instrument laser-machined on an 18 Ga (BWG) SS-316 tube. (a) Schematic side profile depicting tendon placement, presence of the outer sheath or lumen, and actuation DOFs. (b) *Section AA'* - cross-section of the PTFE outer sheath/lumen and (c) An instrumented prototype under arbitrary deflection, depicts laser beam being delivered through the central channel

Rohith Karthikeyan, Shivanand Pattanshetti and Seok Chang Ryu are with the BioRobotics Laboratory in the Department of Mechanical Engineering, Texas A&M University, College Station, TX 77843, USA rohithkarthikeyan, shivanandvp, scryu@tamu.edu

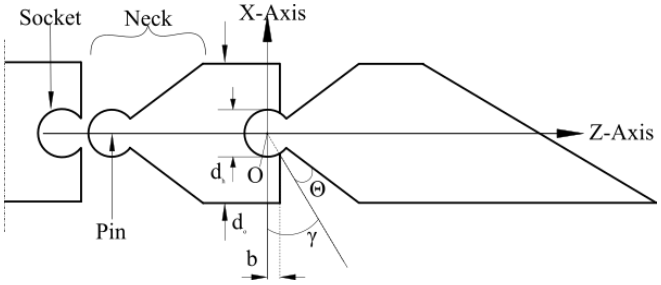

Fig. 2. Exploded schematic of the proposed hinge joint depicting characteristic dimensions as relevant to the description under *Section II*.

this end, we employ thin, needle-scale robotic tubes where tendons actuate the joint. We demonstrate the superiority of the hinge joint in its ability to generate tighter curvatures within limited workspaces, and also study their strength (a perceived drawback) under axial and lateral load. In addition, we illustrate the functionality of the inner working channel by delivering a laser beam to perform path-tracing on a given plane (a proxy for ablation techniques) using simple kinematic control. Based on these observations, we believe that the hinge can be used for the design of sufficiently robust, small-scaled needle-like devices that permit articulation while retaining a functional inner working channel.

The rest of this paper is organized into six sections. ***Section II*** introduces relevant background and ***Section III*** presents the kinematic analysis. In ***Section IV*** we investigate joint strength and in ***Section V*** we explore its function as a delivery platform. ***Section VI*** presents our conclusions.

II. Background

The primary advantage of laser-machined hinge joints is that the machining process permits the fabrication of further miniaturized, monolithic instruments that negate the need for assembly, retain a functional working channel (for drug delivery, tool access, etc.) and enable articulation through a stable joint mechanism. The on-axis machining process to fabricate the hinge does come with limitations, in that, there is a trade-off between strength and range of motion.

The hinge joint consists of three segments – (1) the pin, (2) the hinge socket, and (3) the neck (see 2). Actuation is permitted by the interface between the pin and socket segments. The neck is designed to limit the range of motion for the joint, while it's relative width and the overlap ratio (at the hinge) affect joint rigidity. The relationship between neck width and the joint's range of motion is characterized by the expression for a 2D line equation as below [9]:

$$\tan(\theta_{max}) = \frac{\tilde{y} - \frac{d_h}{2}\sin(\gamma + \theta_{max})}{\frac{d_o}{2}\sin(\frac{\tilde{x}}{d_c/2}) - \frac{d_h}{2}\cos(\gamma + \theta_{max})} \quad (1)$$

where, d_h, d_o, and θ_{max} refer to the hinge width, tube diameter, and maximum intended range of motion respectively, with $\gamma = sin^{-1}(\frac{b}{d_h/2})$. For the scope of this study, we consider three hinge sizes – 40, 50, and 60 %, these ratios are a measure of the hinge width (d_h) normalized with respect to tube diameter (d_o). This paper serves to validate the superior functionality of such rotational hinge joint and their effectiveness in articulate instruments in terms of kinematic simplicity, strength, and function.

III. Kinematic Analysis

A. Hinge and flexure joints: A comparison

A common approach to enable articulation in tools at this scale is through the aid of flexure joints. Patterned superelastic material such as NiTi permit some extent of controlled bending, usually through tendons as transmission media [7], [10]. In this section, we discuss the comparative benefits of hinge-jointed structures over flexures. For the sake of this comparison, we identify two metrics that affect tool manipulation within constrained workspaces – (i) joint deflection (θ) which is directly related to the curvature enabled by the instrument, and (ii) the swept volume (footprint) of the instrument. We discuss the behavior of the hinge and flexure joints using simple (accepted) kinematic approximations. In addition, we limit our focus to laser-machined flexures, in particular, symmetric circumferential slits that alter the stiffness of the tube along its length to enable bi-directional bending. Here, the authors are not inclined toward optimizing slit geometry, and choose instead to adopt from existing literature. It is worth noting that the characteristic dimensions of the slit design however are limited by machining effects and hysteresis.

The kinematics of the flexure can be obtained using a constant curvature assumption as described in [7], with maximum permissible deflection as given by (see Fig. 3 (a)):

$$\theta_{max} = \frac{n.h}{r_o + \bar{y}} \quad (2)$$

where, n is the number of slit segments, r_0 the outer radius of the tube, and $\bar{y}$ the position of the neutral axis.

For the hinge, a simplified relationship between tendon extension and observed deflection can be described using the equation below:

$$\theta = sin^{-1}\left(\frac{h - \Delta L}{S}\right) \quad (3)$$

At the outset, this kinematic expression seems elementary, however, its merit lies in its ability to sufficiently characterize hinge kinematics (a fact demonstrated in ***Section V***).

We make this comparison through two types of constraints – (i) **equivalent axial dimensions (H_j)** for the machined segment (i.e. equivalent swept volume). For the given $H_j = 0.51\ mm$ the hinge is geometrically constrained to enable $\pm 25°$ of deflection (see θ in Fig. 3 (a) [**top**]). Now, for a fair juxtaposition, we adopt the best permissible slit distribution scheme (bi-directional, symmetric) tailored to span the same axial distance H_j. We refer to asymmetric slits in current literature (see Swaney et al. [7]) and scale values to meet the aforementioned constraint (see table in Fig. 3) (a)). The maximum deflection that can be produced by such a flexure is then determined using Eq. 2 and is found to be $\sim 15.15°$. Therefore, for equivalent H_j, the hinge proffers a higher

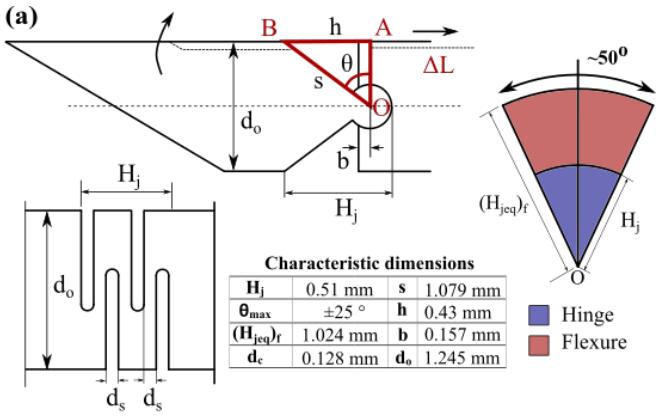

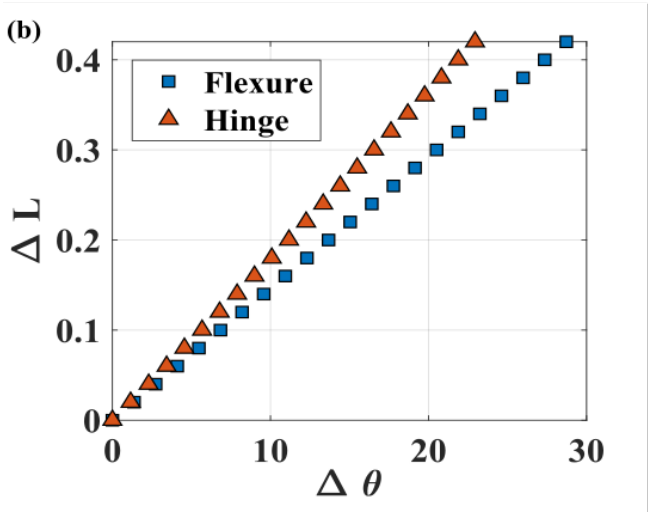

Fig. 3. (a) Schematic of hinge and flexure type joints with equivalent axial dimensions (H_j). Tabular column (**inset**) presents the characteristic dimensions, and a pie-diagram shows the scaled swept area for a flexure and hinge having equal θ_{max} ($\approx 50°$). (b) Plot comparing deflection of flexure and hinge-type joints against tendon extension.

deflection with $\theta_{max} = \pm 25°$. The next constraint is to have joint-dimensions that produce the same $\theta_{max} (= \pm 25°)$, (ii) **equal maximum deflection** ($\theta_{\mathbf{max}}$), – this requires for modifications in either (a) the *flexure geometry* which is hindered by issues such as stress concentration/ machining effects or (b) *flexure distribution* i.e. have a greater number of slits (when retaining the original geometry), which would in turn increase joint length and hence, its swept volume. The pie diagram in Fig. 3(a) illustrates the difference in swept area for the two joints having, with flexure-span $(H_{jeq})_f$ greater than that of the hinge for equal $\theta_{max} (= \pm 25°)$. Clearly, this substantiates our hypothesis in favor of the hinge for compact articulation.

Evidently, hinge joints permit compact articulation, and shorter tip geometries than their flexure counterpart, which is particularly beneficial to minimize unwarranted deviation due to tissue reaction, and also to reduce the overall distal tool footprint. In summary, for minimally invasive surgical applications where there is often a need for tighter curvatures, and small form-factors within spatially limited work-spaces, the hinge provides an advantage over flexure-type joints.

B. Analytical model

The hallmark of hinge joints used in miniature devices is that they enable the use of a simple kinematic model with fewer assumptions than is required for flexure joints. This is due to the rotational nature where the axis remains at the center of the pin. We prepare an analytical model of a robotic arm with two orthogonal laser-machined hinges. We make several simplifying assumptions in our model – (1) the axis of the actuating tendon is assumed to run at a distance equal to the average radius of that tendon away from the surface of the metallic tube that makes up the robotic arm. The outer lumen ensures that the tendon path does not deviate much from this assumption and (2) it is assumed that the tendon runs in straight line segments at all times.

Let $\mathbf{O} = (0\ 0\ 0\ 1)^T$ indicate the local origin of an arbitrary reference frame. The centers of each hinge are determined from the hinge actuation angles (θ_1, θ_2). For a robotic arm with hinges configured in two orthogonal planes (see Fig. 4 (c)), the centers of each hinge and the end-effector are at:

$$\mathbf{P_{O1}} = T_z\,(a_1)\,.O \tag{4}$$

$$\mathbf{P_{O2}} = T_z\,(a_1)\,.\left(R_z\,(\theta_1)\,.T_z\,(a_2)\,.R_z\left(\frac{\pi}{2}\right)\right).O \tag{5}$$

$$\mathbf{P_{EE}} = T_z\,(a_1)\,.\left(R_z\,(\theta_1)\,.T_z\,(a_2)\,.R_z\left(\frac{\pi}{2}\right)\right).O \tag{6}$$

where, T_z is translation along z, and R_z is rotation about z.

Now, a screen in 3D space be represented by the following equation of a plane in 3D, $z = Ax + By + D$. Consider drawing an ellipse on this screen. The equation of an ellipse with l_a, l_b as major and minor axes respectively, in the XY plane to be drawn in time T can be represented as ($\mathbf{P_{exy}}$):

$$\mathbf{P_{exy}} = \begin{pmatrix} l_a \cos(2\pi t/T) \\ l_b \sin(2\pi t/T) \\ 0 \end{pmatrix} \tag{7}$$

The equation of the ellipse on the plane of the screen ($\mathbf{P_e}$) is obtained by transforming Eq. (7). Knowing that the normal to the ellipse on XY plane is given by $\mathbf{n_{exy}} = (0\ 0\ 1)^T$ and the normal to the plane of the screen is given by $\mathbf{n_{screen}} = \left(\frac{-A}{\sqrt{A^2+B^2+1}}\ \frac{-B}{\sqrt{A^2+B^2+1}}\ \frac{1}{\sqrt{A^2+B^2+1}}\right)^T$, we can write the equation of the ellipse on the screen as:

$$\mathbf{V_{cross}} = \mathbf{n_{exy}} \times \mathbf{n_{screen}} \tag{8}$$

$$\mathbf{V_{skew-sym}} = \begin{pmatrix} 0 & -z_{\mathbf{V_{cross}}} & y_{\mathbf{V_{cross}}} \\ z_{\mathbf{V_{cross}}} & 0 & -x_{\mathbf{V_{cross}}} \\ -y_{\mathbf{V_{cross}}} & x_{\mathbf{V_{cross}}} & 0 \end{pmatrix}$$

$$P_e = \mathbf{I_{3\times 3}} + \mathbf{V_{skew-sym}} + \frac{1 - \mathbf{n_{exy}}.\mathbf{n_{screen}}}{\|V_{skew-sym}\|^2}\mathbf{V_{skew-sym}} .\mathbf{V_{skew-sym}}.P_{e_{XY}} + (0\ 0\ D)^T \tag{9}$$

With Eq. 6 and Eq. 9 we can trace elliptical trajectories on arbitrary surfaces using inverse kinematics. We consider

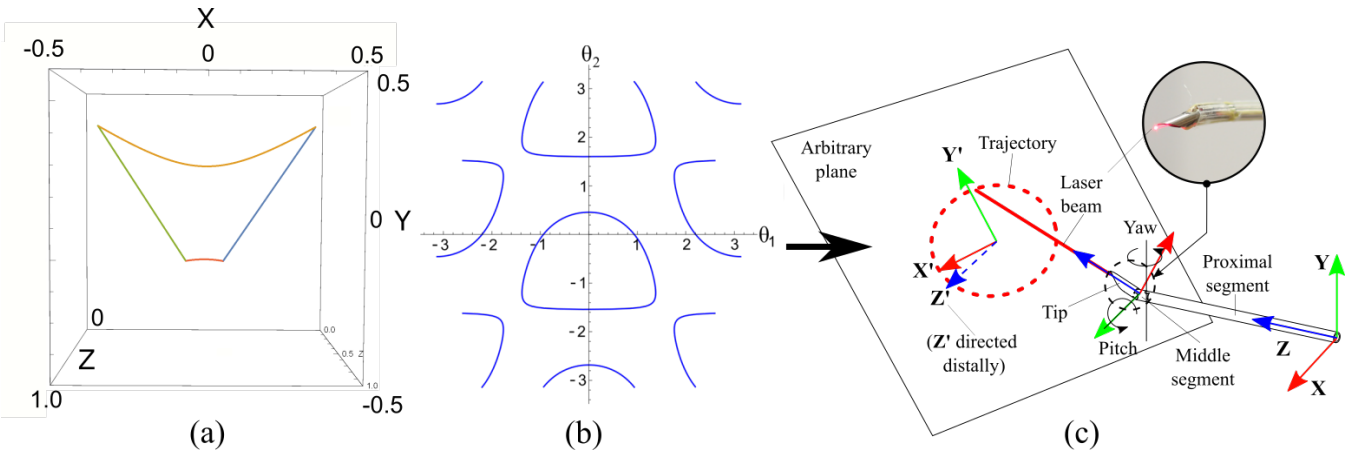

Fig. 4. (a) An illustration of the boundaries of the projected tip on an inclined plane when the hinges are at their actuation limit for a 2-DOF hinge-jointed robotic arm, (b) possible solutions to generate the desired elliptical/ circular trajectory on an arbitrary reference plane with dimensions as described in *Section III*-A, and (c) schematic representation of projection tracing on an inclined surface using a hinge-jointed articulate instrument, **inset:** instrumented robotic arm prototype with optical fiber that delivers the laser-beam, tendons (in yellow) and outer PTFE/ polymer sheath are visible

the case of drawing an ellipse on an arbitrary plane (Fig. 4). Here, we use a laser-beam to trace the desired shape and we term this ***projection tracing***. Now, assuming that the laser beam or the center of the field of view of the endoscope is along the distal tip segment of the robotic arm and extends till the screen, the point on the screen coinciding with this line can be found as the solution of the equation of the screen, and a line continuing in the direction of the distal tip segment given by

$$\frac{x - x_{P_{EE}}}{x_{P_{EE}} - x_{P_{O2}}} = \frac{y - y_{P_{EE}}}{y_{P_{EE}} - y_{P_{O2}}} = \frac{z - z_{P_{EE}}}{z_{P_{EE}} - z_{P_{O2}}} \quad (10)$$

The resulting solution will be the coordinates of the point in 3D as a function of the joint parameters θ_1, θ_2 (see Fig. 4 (b)) and the screen parameters A, B, and D.

$$P_{pt\_on\_screen} = f_1(\theta_1, \theta_2, A, B, D) \quad (11)$$

The inverse kinematics can be computed by inverting the above equation to give the joint parameters θ_1 and θ_2 in terms of the coordinates of the point on screen (Fig. 4 (b)).

These parameters are in terms of the X, Y, and Z coordinates of the point on screen. Since the end-effector has to trace the ellipse above, the parametric equations for the ellipse in terms of time(t) can be substituted in place of x, y, and z. Based on the analytical model, the tendon length change is mostly beside the hinge joints. Therefore, the desired joint coordinates are then converted into appropriate tendon displacement parameters using Eq. 3. In ***Section V*** we demonstrate the validity of the proposed projection tracing technique by considering a simplified circular geometry on an arbitrary plane offset from the instrument's tip.

IV. Characterizing Hinge Strength

Due to the absence of a physical connection between the socket and pin there are concerns about the strength of such hinge joints. We look to dispel this perceived demerit by studying the load thresholds of the hinge under different conditions. Here, we define two measures for hinge strength – (1) *axial strength*, defined as the ability of the socket to prevent pin dislocation and retain a secure fit under axial loading (synonymous to needle retraction events), and (2) *lateral strength*, defined as the ability of the socket to constrain the pin against failure due to lateral load at the tip (a proxy for tissue reaction).

A. Test Specimen

We consider two types of specimen – (a) the *tube*, a laser-machined structure with an embedded single-DOF hinge joint and (b) the *prototype*, a skeletal *tube* with tendons that reinforce the hinge and a polymer outer lumen (see Fig. 4 (c) (inset)). An antagonistic pair of tendons actuate the hinge, while the lumen ensures that tendon position is constrained.

We test three different hinge sizes - 40, 50 and 60 % (see *Section II*) that could provide an optimum trade-off between their range of motion and estimated strength. The choice of material include, thin-walled and thick-walled medical grade stainless steel (SS 316), and super-elastic NiTi alloy. Further, to better represent the capabilities of the hinge, we limit our tests to small-sized tubes comparable to an 18 Ga (BWG) medical needle, whose wall thickness was between 0.127 mm and 0.1524 mm in order to estimate a lower-bound for the aforementioned strength attributes.

B. Methods

We performed lateral and axial loading tests on *tube* and *prototype* specimen using custom-designed rigs atop an optical breadboard as indicated in Fig. 5. During these tests, the specimen were constrained by a three-jaw chuck (Dremel 4486) affixed to a 3D printed block. The tendon arrangement was varied contingent on the loading direction (axial: Fig. 5 (a) or lateral: Fig. 5 (c)). One end of each tendon was tethered to a 6-axis F/T sensor (ATI Nano 17, ATI Industrial Automation, Apex, NC, USA) using a 3D printed interface. The force sensor was mounted on top of a micrometer-driven, single-axis translation stage (Thorlabs, Newton, NJ, USA). Stage displacement was used to vary the tendon tension and in-turn the joint load. Three *prototypes* and *tubes* were tested

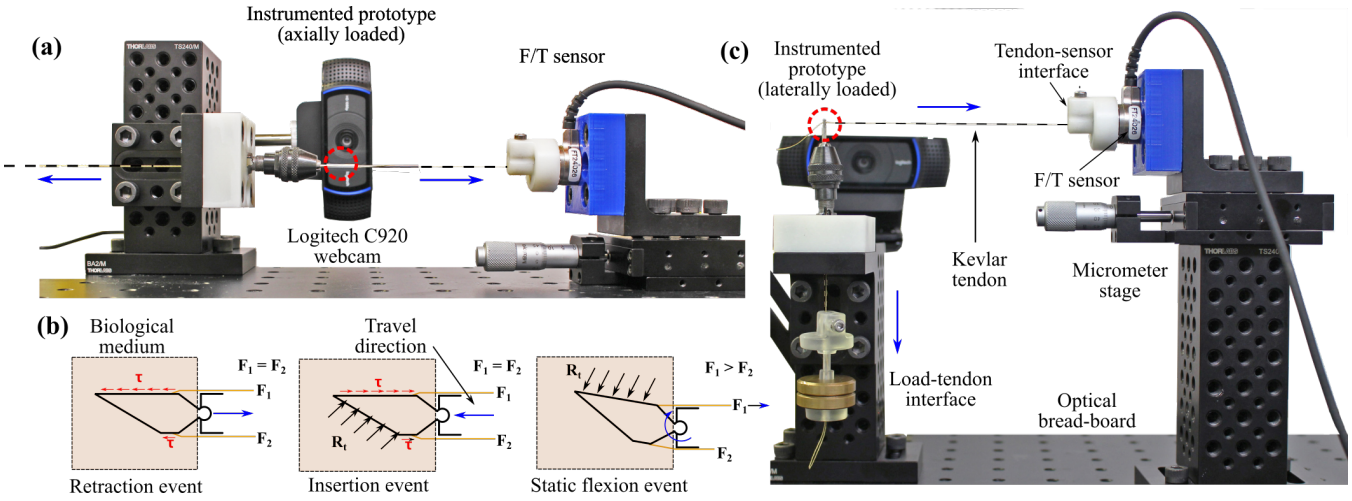

Fig. 5. Experimental setup for strength experiments on hinge-jointed specimen, with the workpiece constrained by a three-jawed chuck on a 3D printed fixture. (a) Axial strength test setup shows the workpiece loaded in the axial direction and pre-tensioned by weights (not pictured) at the proximal end, (b) Common loading configurations for instruments during in vivo manipulation, and (c) lateral force test setup shows the specimen tethered to the F/T sensor and pre-tensioned by weights suspended at the proximal end.

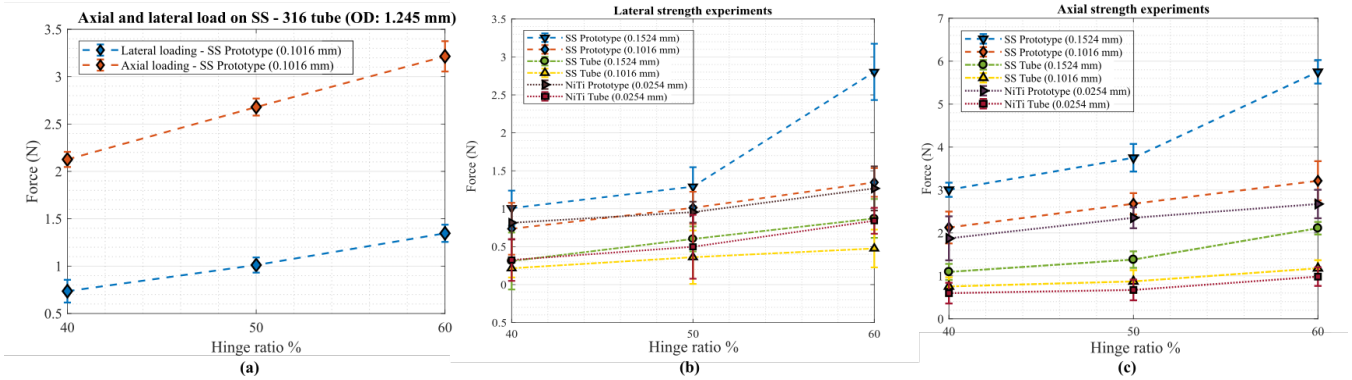

Fig. 6. Plots depict load at failure for tube and prototype specimen under axial and lateral loading conditions. The plots compare the performance of SS-18XT316 (thin-walled), SS-18XTW316 (thick-walled) and Nitinol tube of comparable sizes. The prototypes are reinforced by the tendons (40 g tensile load) and lumen. (a) Super-imposed plots for axial and lateral load on SS-316 *prototype* (0.1016 mm), (b) lateral strength data, and (c) axial strength data.

for each hinge configuration, where, the micrometer was actuated in step-wise increments until specimen failure (i.e. hinge dislocation). A feature tracking algorithm was used to ascertain the exact point-in-time for specimen failure from recorded video.

C. Discussion on strength data

The plots in Fig. 6 summarize the results obtained from the experiments described in Section IV-B. Each data point corresponds to the average of three (or more) trials, with whiskers depicting their standard deviation. Under lateral load at the distal end (see. 5 (c)), the thin-walled SS-316 *tubes* registered a failure load of 0.215 N, for 40 % hinge sizes, the lowest among the specimen considered. The thick-walled SS-316 *prototypes* registered a failure load of 1.007 N at 40% and up to 2.803 N at 60 % hinge sizes – the maximum observed among the material-types and dimensions considered. The axial strength experiments show trends similar to that under lateral load, however, the pin-socket interface appears to be considerably stronger for axial loading. This is reasonable given that the design of the hinge ensures a better fit for the interface along the tube axis. Again, the SS-316 thick-walled *prototype* and *tube* show significantly higher load bearing capacities that varied between 1.0927 N (40 % *tube*) and 5.753 N (60 % *prototype*). Notably – (1) there was considerable deviation in the measured values for the 40% hinge size across all variables – this can be attributed to its inherent fragility and tendency to dislocate during instrumentation; (2) the *prototypes* show a greater resistance to failure due to the reinforcing effect introduced by the tendon and outer lumen, and (3) in all observations, failure was characterized by reversible hinge dislocation and no fracture or plastic deformation at the pin-socket interface. Importantly, these results indicate that hinge strength appears to be a function of hinge size, and wall-thickness with the SS-316 thick-walled *prototype* offering an optimum trade-off between device scale and the required range of motion.

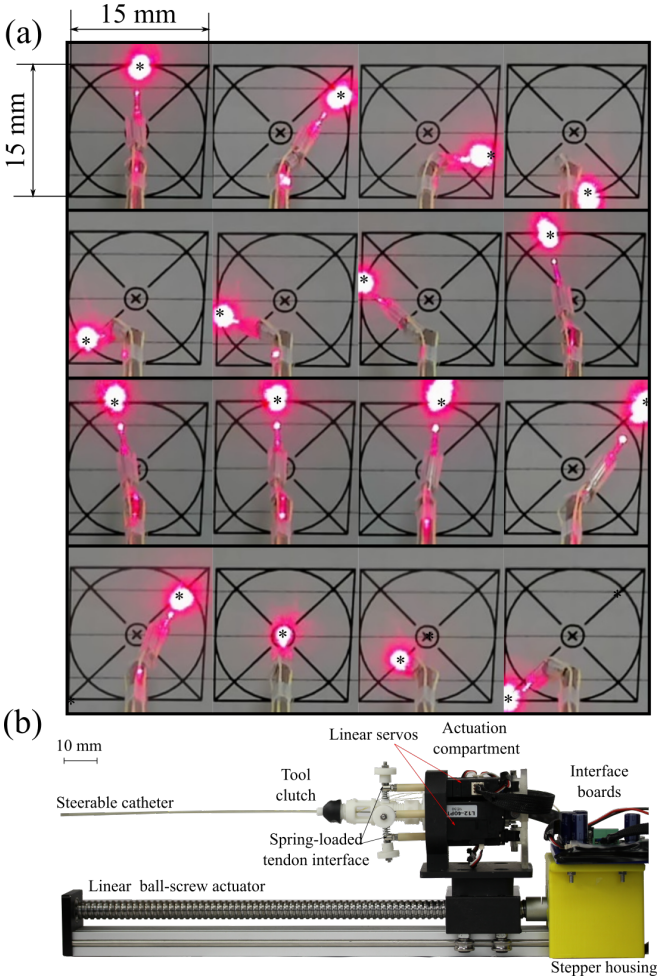

Fig. 7. Projection tracing using an optical fiber: (a) Montage of laser-beam tracing a circle on an arbitrary plane offset from the instrument's tip, where asterisks denote the desired position. Sequence organized L-R by row, and (b) the driving system used for kinematic validation and path tracing.

V. Feasibility as Delivery Platform

In order to demonstrate the utility of hinge-jointed articulate instruments for the delivery of drugs, tools, or optical fibers, we undertake path-tracing experiments using the methods discussed in ***Section III-B***. Here, an optical fiber delivering a laser beam serves as a proxy for functionally similar tools that can be introduced into the body through the working channel of the proposed instrument.

We demonstrate this capability by tracing a circle of diameter $15\ mm$ and a square of side $15\ mm$ on a plane at an offset distance of $5\ mm$ from the instrument's tip. These dimensions are constrained by the focusing distance of the laser-beam, and the tube's workspace. The robotic tube is equipped with a coaxial, single mode, pig-tailed optical fiber which was stripped to expose its core (LC/APC 9/125 FS.COM, Renton, WA). The end of the optical fiber was positioned close to the needle's tip and it delivers the laser-light from a visual fault locator ($20\ mW$ FVFL-209, FS.com, Renton, WA) that is interfaced to the fiber connector. The laser-beam incident on the plane is used to trace the aforementioned 2D geometries. The experimental procedure can be broken into the following rudiments, first, the desired end-effector position is obtained and the corresponding joint coordinates are determined through the inverse kinematics solution for the robot's configuration. The joint coordinates are then converted to appropriate tendon-displacement primitives. These displacement parameters are scaled, and fed to a servo-controller on-board the actuation platform (see Fig. 7 (b)). The pre-tensioned instrument is then displaced to the specified configuration.

Here, a software application feeds the desired tendon-displacements in a sequential manner to obtain the end-effector positions as shown in Fig. 7 (a). A web-camera (Logitech Brio 4K ultra HD Wsebcam, Logitech, Newark,CA) mounted atop the driver was used to video-graph tip-position during run-time. From the figures, the kinematic-controllability of the hinge is evident. Notably, for the circle-tracing activity shown the RMS of positioning error was approximately $0.364\ mm$. This demonstration reinforces the functionality of the hinge as a reliable delivery platform in intervention modes that demand targeted laser-ablation.

VI. Conclusion

Rotational hinge joints fabricated on a tubular structure are potential alternatives to the widely used flexures, especially for smaller steerable devices in medical applications that require a functional working channel. However, the expected advantages over its counterpart were not studied previously.

The kinematic analysis performed in ***Section III-A***, under the specified set of assumptions, proves that hinge joints permit finer angular positioning resolution and shorter joint lengths. Therefore, such joints could lead to reduced tip-positioning error in small-scaled steerable catheters due to the diminished effect of tissue reaction at the instrument tip, while retaining full orientation control of the distal segment. However, the hinge joint has a drawback in the form of its strength, which can be attributed to the lack of physical connections between each part (see Fig. 2). In ***Section IV***, we determined a lower bound for the joint strength of an $18\ Ga$ needle size NiTi tube under expected loading conditions. Our observations indicate that, while it is inherently weaker than a flexure, the estimated strength is sufficient for the joint to deliver common materials and devices, especially when assembled with the actuating tendons and a guiding outer lumen (*prototype*).

The authors prototyped a needle-sized robotic arm with 2-DOF hinge joints at the tip and an optical fiber, in order to evaluate the simple kinematic model developed in ***Section III-B***. The results demonstrate that the intuitively simple model is sufficient to describe tip motion, which isn't possible for flexure joints which are generally impeded by material nonlinearity, and issues arising from geometric discontinuities and resulting stress concentrations. Thus, the proposed robotic tube with rotational tip joints is promising as a small-scale delivery platform. In the future, it will be applied to emerging medical techniques such as laser surgery, ablation, and targeted drug delivery.

REFERENCES

[1] H. Schreuder and R. Verheijen, "Robotic surgery," *BJOG: An International Journal of Obstetrics & Gynaecology*, vol. 116, no. 2, pp. 198–213, 2009.

[2] C. Bergeles and G.-Z. Yang, "From passive tool holders to microsurgeons: safer, smaller, smarter surgical robots," *IEEE Transactions on Biomedical Engineering*, vol. 61, no. 5, pp. 1565–1576, 2014.

[3] A. Degani, H. Choset, B. Zubiate, T. Ota, and M. Zenati, "Highly articulated robotic probe for minimally invasive surgery," in *Engineering in Medicine and Biology Society, 2008. EMBS 2008. 30th Annual International Conference of the IEEE*, pp. 3273–3276, IEEE, 2008.

[4] N. Simaan, K. Xu, W. Wei, A. Kapoor, P. Kazanzides, R. Taylor, and P. Flint, "Design and integration of a telerobotic system for minimally invasive surgery of the throat," *The International journal of robotics research*, vol. 28, no. 9, pp. 1134–1153, 2009.

[5] S. Mattheis, P. Hasskamp, L. Holtmann, C. Schäfer, U. Geisthoff, N. Dominas, and S. Lang, "Flex robotic system in transoral robotic surgery: the first 40 patients," *Head & neck*, vol. 39, no. 3, pp. 471–475, 2017.

[6] P. E. Dupont, J. Lock, B. Itkowitz, and E. Butler, "Design and control of concentric-tube robots," *IEEE Transactions on Robotics*, vol. 26, no. 2, pp. 209–225, 2010.

[7] P. J. Swaney, P. A. York, H. B. Gilbert, J. Burgner-Kahrs, and R. J. Webster, "Design, fabrication, and testing of a needle-sized wrist for surgical instruments," *Journal of medical devices*, vol. 11, no. 1, p. 014501, 2017.

[8] N. E. Bruns, O. S. Soldes, and T. A. Ponsky, "Robotic surgery may not "make the cut" in pediatrics," *Frontiers in pediatrics*, vol. 3, 2015.

[9] S. Pattanshetti and S. C. Ryu, "Design and fabrication of laser-machined hinge joints on miniature tubes for steerable medical devices," *Journal of Mechanisms and Robotics*, vol. 10, no. 1, p. 011002, 2018.

[10] S. C. Ryu, P. Renaud, R. J. Black, B. L. Daniel, and M. R. Cutkosky, "Feasibility study of an optically actuated mr-compatible active needle," in *Intelligent Robots and Systems (IROS), 2011 IEEE/RSJ International Conference on*, pp. 2564–2569, Ieee, 2011.